Exploring the chemical interactions of lead(II) oxide and linseed oil in historical and model paint systems using laboratory and safe synchrotron radiation analysis

Fazlić, I.

Publication date
2025

Chapter 1 Introduction

Oil paint consists of finely ground pigment dispersed in an organic oil binder. Upon exposure to air, the oil binder undergoes a series of chemical reactions - known as curing reactions – that gradually harden the paint film [1, 2]. These chemical reactions of the oil occur slowly under ambient conditions unless promoted by a drier, (ultraviolet, UV) light or elevated temperature [2-4] . Driers, particularly lead(II) oxide (PbO), not only promote the curing reactions of oil, but also chemically interact with the oil components, resulting in the formation of complex reaction products [5-9]. Chemical research of historical paintings conducted over recent decades has confirmed that these lead-based products become integrated into the paint structure [7, 10]. Given that oil is a large part of oil-based paints, the interactions between drier-binder influence the paint's physical and chemical properties, overall stability, and response to environmental factors and conservation treatments. This thesis specifically examines the chemical interaction of linseed oil (LO) and PbO drier, with a focus on the reaction pathways and product formation through historical and model systems.

1.1 Composition of oil

Oil primarily consists of triacylglycerols (TAG) and a mixture of various types of unsaturated and saturated fatty acids. TAGs consist of three (un)saturated fatty acids. A large number of combinations of fatty acids in TAGs exists. The most abundant unsaturated fatty acids in painting oils are: oleic (C18:1), linoleic (C18:2), linolenic (C18:3), palmitoleic (C16:1) and α-elaeostearic acid (α-C18:3), while the saturated ones are palmitic (C16:0), stearic (C18:0). Smaller amounts of unsaturated fatty acids: palmitoleic (C16:1) and gondoic acid (C20:1) and saturated fatty acids: lauric (C12:0), myristic acid (C14:0), arachidic acid (C20:0), behenic acid (C22:0) and lignoceric acid (C24:0) can be found in oil binders [2, 11, 12].

1.1.1 Classification of oils

Oils are classified as non-drying, semi-drying or drying oils based on their unsaturated fatty acid content, which determines their ability to react with oxygen and polymerize [2, 11]. Drying oils, such as linseed, walnut and poppyseed oil are widely used in historical paintings as they form a strong, durable film. Semi-drying (sunflower and cottonseed) and non-drying (rapeseed and castor) oils do not fully form a solid film upon exposure to oxygen, which is why they were generally avoided in traditional painting techniques. In modern oil paint, semi- and non-drying oils became more commonly used, after modification by heat, addition of driers or by mixing with drying oils [13-18].

The drying power of oil is defined by the iodine value (IV). Unsaturated fatty acids are particularly reactive to iodine. The iodine value is expressed by the grams of iodine necessary to saturate the double bonds of 100 grams of oil. If the iodine value of an oil is greater than 140, it is considered to be a drying oil. An iodine value between 125 and 140 classifies the oil as a semi-drying, and an iodine value lower than 125 makes it a non-drying oil. IV may also be calculated based on the formula:

$$1.16\ IV = 3.04\ (\%\ \text{linolenic acid}) + 2.02\ (\%\ \text{linoleic acid}) + (\%\ \text{oleic acid})$$ [2, 11, 19, 20].

In addition to IV, another way to determine the drying power of an oil is through the drying index, calculated for the non-conjugated double bond fatty acid chains. Precisely, to be classified as a drying oil, the drying index value should be greater than 70 [2, 11]. The drying index is calculated by the following formula:

$$\text{Drying index} = (\%\ \text{linoleic acid}) + 2\ (\%\ \text{linolenic acid}).$$

Non-conjugated double bonded fatty acids are more reactive to oxygen than conjugated double bonded fatty acids due to the methylene interruption. The bis-allylic hydrogen in the methylene group is easily abstracted due to low bond C-H dissociation energy, which leads to the initiation of radical chain reactions and autoxidation [21]. An example of a non-conjugated fatty acid containing, drying oil used in painting domain is LO, which contains 68% of non-conjugated *cis*-CH=CH-double bonds [2, 22].

1.1.2 Linseed oil (LO)

LO is derived from flax seed (*Linum usitatissimum*). Flax seed is grown on all continents and type of flax and final composition of the TAGs depend on the geographical provenance, climate conditions and farming and production process of LO. Flax can give oleaginous (linseed) and textile (fibre) flax. There are two methods of oil production, used until today: pressure method and solvent extraction. For both methods, the seeds are first cleaned and separated by blowing air or screening. The seeds are then ground and heated to coagulate the proteins in the walls of the cells and lower the viscosity of the oil, which enables it to flow from the seeds. In modern production, solvents are used to extract more oil. LO is classified as a drying oil due to its high content of unsaturated fatty acids. Its primary components are TAG and varying amounts of saturated (C12:0 lauric, C14:0 myristic, C16:0 palmitic or C18:0 stearic fatty acid) and mono- (oleic C18:1) and polyunsaturated fatty acids (linoleic fatty acid C18:2 and linolenic fatty acid C18:3) mixtures. Compared to other drying oils like walnut or poppyseed, LO has the highest linolenic acid content, making it highly reactive in autoxidation, the oxygen-driven polymerization process [2, 12, 23, 24]. Due to its high linolenic acid content, LO undergoes curing reactions which form a stable film that made it the preferred binder and protective layer in historical oil paintings [12].

1.2 Curing of oil

To facilitate understanding of the chemical interactions between PbO and LO and their reaction products, it is helpful to first review the curing reactions of LO in the absence of driers. Curing reactions refer to the overall hardening of the oil, occurring through autooxidation reactions.

1.2.1 Autoxidation reaction

Autoxidation of lipids in the oil is a complex process due to the multiple concurrent chemical pathways. However, previous research has successfully identified and described the key reaction mechanisms, which can be broadly categorized into the three phases: initiation, propagation, and termination [21, 25-33].

Initiation

During initiation, an allylic ($-CH_2-HC=CH_2$) or bis-allylic hydrogen is abstracted by the reaction with oxygen, forming a carbon-centered radical. Figure 1a shows bis-allylic hydrogen abstraction from C11 position of linoleic fatty acid. Hydrogen abstraction and carbon radical formation will occur more readily at lower bond dissociation energies (BDEs) of bis-allylic than allylic C–H bonds in fatty acids [20, 25]. Linoleic acid (18:2) and linolenic acid (18:3) have lower BDEs of ~335 kJ/mol and ~337 kJ/mol, respectively, at their bis-allylic C-H at C11, while oleic acid (18:1) has a BDE of ~361 kJ/mol at allylic C–H at C11 [22, 34]. Hydrogen abstraction leads to the formation of a bis-allylic radical (Figure 1b). This radical then undergoes π-bond rearrangement to form an allylic radical on either C9 or C13 position of linoleic fatty acid and the unconjugated C=C–C–C=C double bonds convert into a conjugated C=C–C=C–C diene. Figure 1c shows an allylic radical formation on the C9 position. The conjugation additionally lowers the energy of the system and makes it more reactive to oxygen [21]. Additionally, isomerization of the C=C bonds leads to the formation of more thermodynamically stable *trans-trans* than *cis-trans* conjugated double bonds, due to the presence of carbon radicals near the unsaturations (Figure 1c) [2, 11, 31].

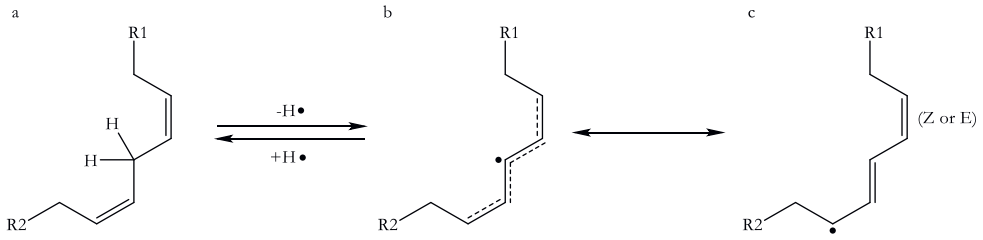

Figure 1. Reaction scheme of oxidation reaction of linoleic fatty acid ($C_{18}H_{32}O_2$). R1 represents the $-(CH_2)_3-CH_3$ part of the molecule and R2 represents $-(CH_2)_6-COOH$ part of the molecule. The figure shows: a) abstraction of a bis-allylic hydrogen from C11 position in linoleic fatty acid; b) formation of a bis-allylic radical; c) rearrangement of bis-allylic radical to form an allylic radical and a conjugated diene and isomerization of the bonds to (*cis*) Z or (*trans*) E geometric configuration. The reaction scheme was created based on literature [2, 8, 23, 30, 33].

Propagation

In this phase, radical intermediates further react, forming new radicals and reaction products. This free radical chain reaction consists of several steps, including radical coupling with oxygen, atom or molecule transfer, fragmentation, rearrangement, and cyclization [2].

The newly-formed carbon-centered, allylic radical (Figure 2a) may react with biradical molecular oxygen, leading to the formation of a peroxyl radical (R-O-O·) (Figure 2b). This peroxyl radical may further react with a hydrogen abstracted from another molecule to form primary oxidation products - hydroperoxides (R-OOH) (Figure 2c) [2].

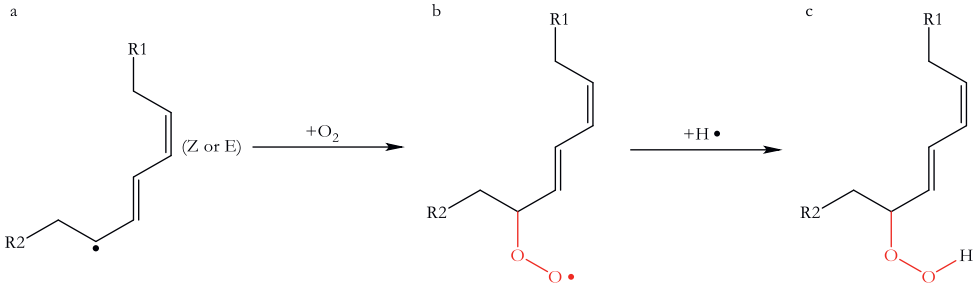

Figure 2. Reaction scheme of oxidation reaction of linoleic fatty acid ($C_{18}H_{32}O_2$). R1 represents the $–(CH_2)_3–CH_3$ part of the molecule and R2 represents $–(CH_2)_6–COOH$ part of the molecule. The figure shows: a) newly formed carbon-centered, allylic radical in Z or E geometric configuration; b) allylic radical reacting with oxygen to form a peroxyl radical (R-O-O·); c) peroxyl radical abstracting H and forming primary hydroperoxides (R-OOH). The reaction scheme was created based on literature [2, 8, 23, 30, 33].

Hydroperoxides (R-OOH, Figure 3a) may decompose again to form a peroxyl radical (R-O-O·) (Figure 3b) or an alkoxy (R-O·) radical (Figure 3c) [30]. The decomposition of hydroperoxides can be influenced by elevated temperature or drier addition (further discussed in Section 1.3).

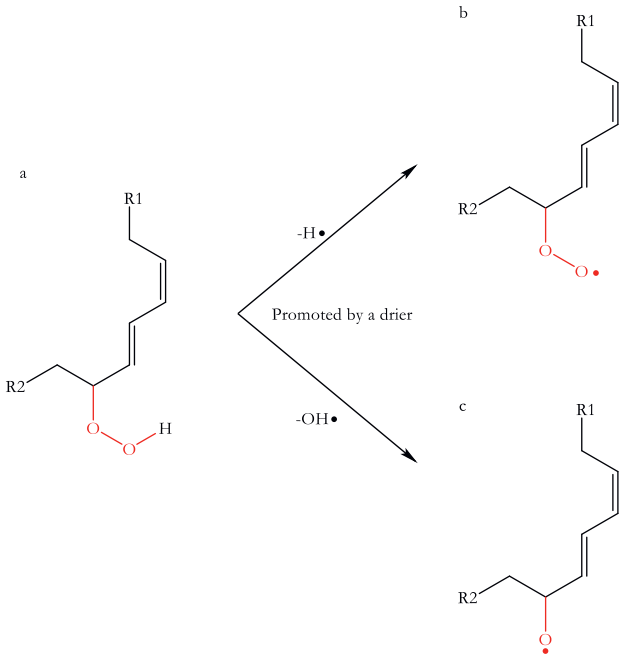

Figure 3. Reaction scheme of oxidation reaction of linoleic fatty acid ($C_{18}H_{32}O_2$). R1 represents the $–(CH_2)_3–CH_3$ part of the molecule and R2 represents $–(CH_2)_6–COOH$ part of the molecule. The figure shows: a) an unstable primary hydroperoxide decomposing to b) peroxyl radical again (R-O-O·) or c) alkoxy radical (R-O·). This reaction can be promoted by a drier (described in Section 1.3) [11, 20, 21, 25]. The reaction scheme was created based on literature [2, 8, 12, 35].

Termination: Polymerization, cross-linking and film formation

While alkoxy radicals can abstract hydrogen atoms to regenerate hydroperoxides, two peroxyl radicals (2R-O-O·) can recombine through Russell termination mechanism and form cross-linked compounds (R-O-O-R + O_2) [2]. Additionally, oligomeric and polymeric compounds (ROOR) may also form by β scission and direct recombination of: i) R-O-O· and R·; ii) R· and R-O-O·, and iii) 2R-O·[2]. Three types of cross-links can exist in the final polymer: C-C, C-O-C and C-O-O-C [11, 22]. Such cross-linking increases the average molecular weight of the oil, ultimately producing a solid, polymerized film [2, 11, 12, 20, 36]. This polymerized network is essential for the long-term stability of oil paints, influencing their resistance to degradation, cracking, and stronger chemical alterations over time.

Secondary oxidation reactions

Besides the initial reactions leading to the formation of primary oxidation products – hydroperoxides – alkoxy and peroxyl radicals (Figure 3) participate in many cascade oxidation reactions to form secondary oxidation products. Secondary oxidation products include numerous volatile products such as aldehydes, ketones, alcohols, and non-volatile cross-linked products, such as epoxides and carboxylic acids [8, 12, 19, 30, 31, 37]. In the following section we will discuss the formation of both volatile and non-volatile secondary oxidation products. More specifically, we will focus on the pathways that lead to the formation of formic acid, which is relevant for further understanding of the chemical reactions discussed in Chapters 2 and 4.

Alkoxy radicals (R-O·, Figure 4a) formed from hydroperoxide decomposition can go through β fragmentation and form unsaturated aldehydes (R1-CH=CH-CH=CH-CHO, Figure 4b) [8, 33, 37].

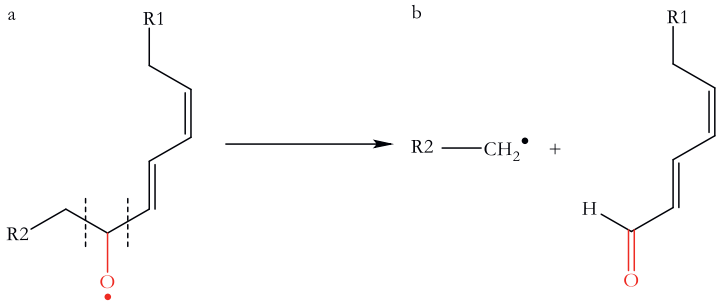

Figure 4. Reaction scheme of oxidation reaction of linoleic fatty acid ($C_{18}H_{32}O_2$). R1 represents the $–(CH_2)_3–CH_3$ part of the molecule and R2 represents $–(CH_2)_6–COOH$ part of the molecule. The figure shows: a) alkoxy radical (R-O·) fragmenting to form b) unsaturated aldehydes (R1-CH=CH-CH=CH-CHO) The reaction scheme was created based on literature [8, 33, 37].

The newly formed carbon-centered radical (R2-CH_2·, Figure 5a) can further oxidise to form peroxyl radicals (R-O-O·, Figure 5b). These peroxyl radicals form a hydroperoxide (R2-CH_2OOH, Figure 5c) which decomposes to alkoxy radicals (R-O·, Figure 5d). The newly formed alkoxy radical can then form saturated aldehydes (R2-CHO, Figure 5e) and formaldehyde (HCHO, Figure 5f) [8, 33, 37]. Furthermore, Švarcová *et al.* (2020) propose further oxidation of formaldehyde to formic acid (HCOOH, Figure 5g) [8].

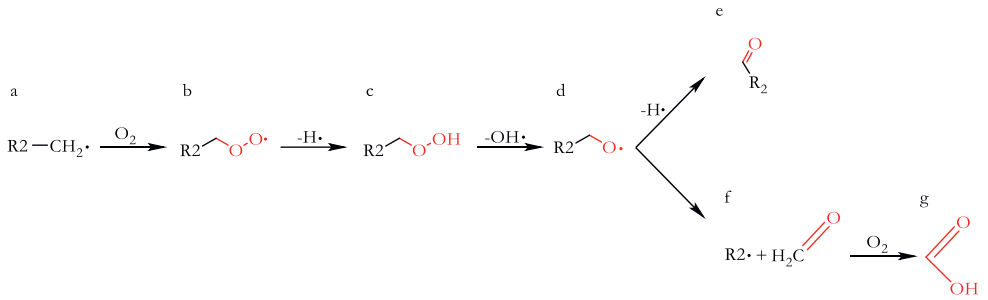

Figure 5. Reaction scheme of oxidation reaction of linoleic fatty acid ($C_{18}H_{32}O_2$). R1 represents the –$(CH_2)_3$–CH_3 part of the molecule and R2 represents –$(CH_2)_6$–COOH part of the molecule. The figure shows: a) a carbon-centered radical (R2-CH_2·) oxidising to b) a peroxyl radical (R-O-O·), which forms c) a hydroperoxide (R2-CH_2OOH). This hydroperoxide then decomposes to d) an alkoxy radical (R-O·). The newly formed alkoxy radical then oxidises to e) a saturated aldehyde (R2-CHO) and f) a formaldehyde (HCHO). Finally, formaldehyde can oxidise to g) formic acid (HCOOH). The reaction scheme was created based on literature [8, 33, 37].

Wexler (1964) proposes another pathway to the formation of formic acid from the opening of the ring of cyclic compounds [33]. First, we will discuss how cyclic compounds form by the autoxidation reactions of oil. Cyclic compounds are formed by the reaction of alkoxy radicals (R–O·, Figure 6a) with double bonds within the same fatty acid chain to form epoxide rings (–C–O–C–, Figure 6b) [20, 21, 31, 38]. In addition to this intramolecular mechanism, epoxides can also form through the addition of peracids (R-COOOH) [20] or peroxyl radicals (R-O-O·) to the carbon-carbon double bonds [21, 24].

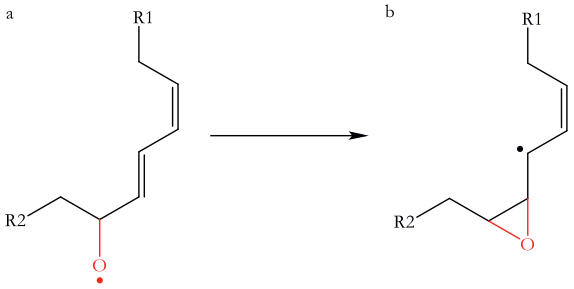

Figure 6. Reaction scheme of oxidation reaction of linoleic fatty acid ($C_{18}H_{32}O_2$). R1 represents the –$(CH_2)_3$–CH_3 part of the molecule and R2 represents –$(CH_2)_6$–COOH part of the molecule. The figure shows: a) an alkoxy radical (R–O·) forming b) an epoxide (–C–O–C–). The reaction scheme was created based on literature [21, 38].

In some cases, peroxyl radicals (R–O-O·, Figure 7a) located near conjugated double bonds can react with the double bonds to form five- or six-membered rings: endoperoxides (Figure 7b). These cyclic structures are sterically unstable and have momentary existence [26].

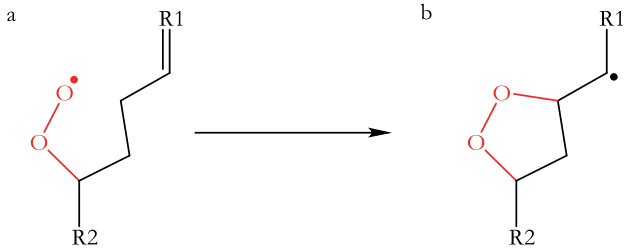

Figure 7. Reaction scheme of oxidation reaction of linoleic fatty acid ($C_{18}H_{32}O_2$). R1 represents the $–(CH_2)_3–CH_3$ part of the molecule and R2 represents $–(CH_2)_6–COOH$ part of the molecule. The figure shows: a) a peroxyl radical (R–O-O·) forming b) an endoperoxide (five- or six-membered ring formation). The reaction scheme was created based on literature [2, 21, 26, 33].

Besides endoperoxides, ozonide-like cyclic compounds can form during oxidation reactions (Figure 8a) [8, 33]. Chiniwalla *et al.* (2002) report that oxygen in these ring structures can react with H_2O (Figure 8a), which causes ring opening (Figure 8b) and formation of a hydroxyl and a free radical (Figure 8c) [20, 33, 39]. Oxygen free radicals can recombine with free radicals of other fatty acid chains, leading to cross-linking and formation of oligomeric and polymeric structures [11, 20, 21, 33, 39]. Furthermore, Wexler (1964) suggests that these free radicals can also react to form formic acid (HCOOH in Figure 8d) or longer chain carboxylic acids (R1-COOH in Figure 8e) [33].

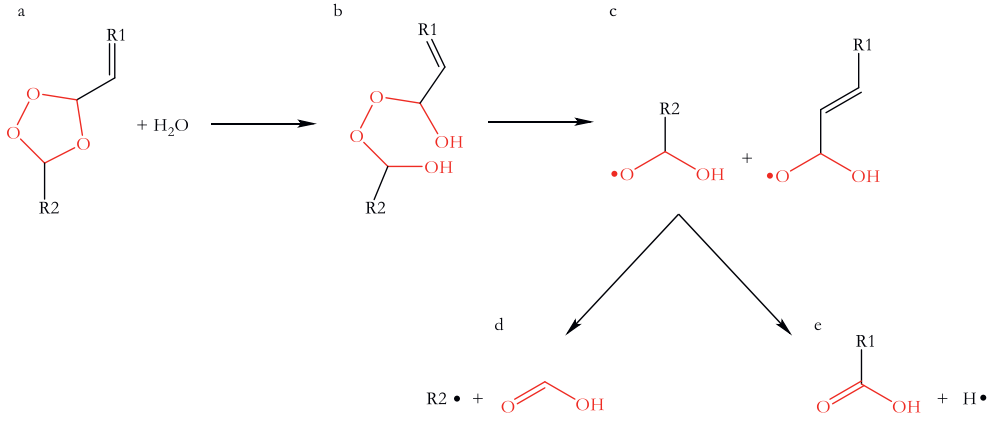

Figure 8. Reaction scheme of oxidation reaction of linoleic fatty acid ($C_{18}H_{32}O_2$). R1 represents the $–(CH_2)_3–CH_3$ part of the molecule and R2 represents $–(CH_2)_6–COOH$ part of the molecule. The figure shows: a) ozonide-like structure reacting with H_2O; b) ring opening; c) free radical and a hydroxyl group; d) formation of formic acid (HCOOH) and e) carboxylic acids (R1-COOH). The reaction scheme was created based on Wexler (1964) [33].

Carboxylic acids (Figure 9e) can also form from oxidation reaction of unsaturated aldehydes (Figure 9d) [37].

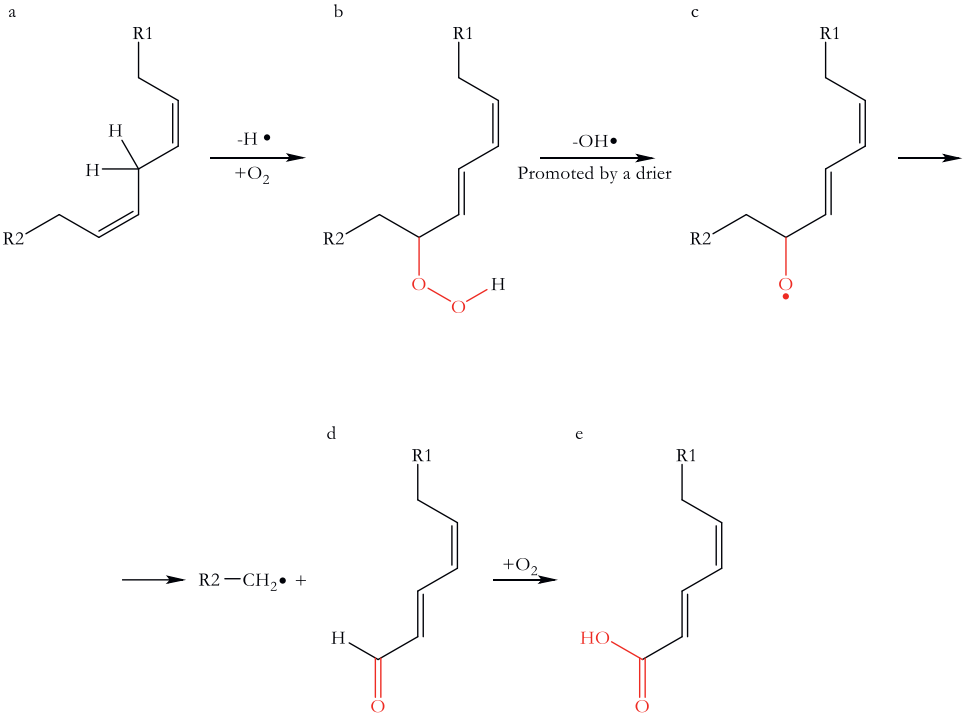

Figure 9. Reaction scheme of oxidation reaction of a) linoleic fatty acid ($C_{18}H_{32}O_2$). R1 represents the $–(CH_2)_3–CH_3$ part of the molecule and R2 represents $–(CH_2)_6–COOH$ part of the molecule. The figure shows formation of: b) hydroperoxides (R-COOH); c) peroxyl radicals (R–O-O·); d) unsaturated aldehydes (R1-CHO) and further oxidation to e) carboxylic acids (R1-COOH). The reaction scheme was created based on literature [2, 8, 11, 37].

In addition to oxidation reaction, free fatty acids (Figure 10b) and glycerol may also form through hydrolysis - a water-induced breakdown of triglyceride ester bonds [1, 2, 37, 40, 41].

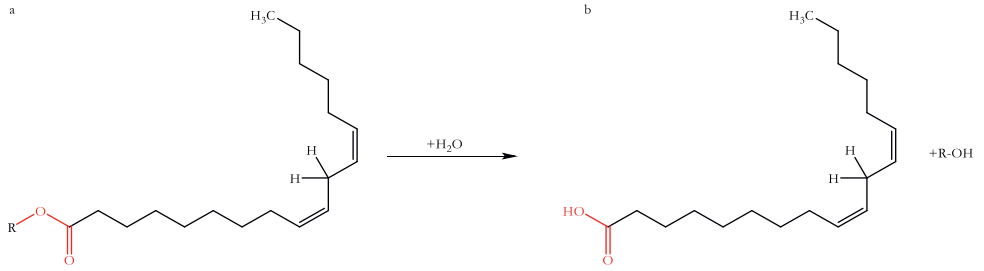

Figure 10. Reaction scheme of hydrolysis reaction of: a) an esterified linoleic fatty acid (R–COO–$C_{18}H_{32}$) leading to the formation of b) free fatty acid ($C_{18}H_{32}O_2$) and alcohols (R-OH). The reaction scheme was created based on Baij *et al.* (2019) [37].

Glycerol and lower molecular weight compounds may evaporate, while oxidised and hydrolysed carboxylic acid groups react with metal ions (coming from the pigment and/or the binder) to form metal carboxylates [6, 42]. These metal carboxylates remain embedded in the cross-linked film, forming a polyanionic ionomer, which may influence the mechanical and chemical properties of the film (Figure 11) [1, 2, 37, 40, 43, 44].

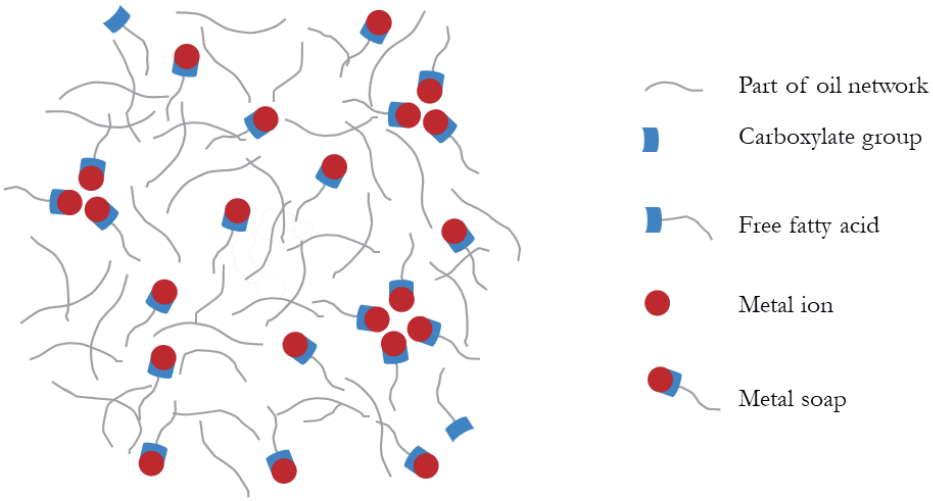

Figure 11. Schematic model showing a paint ionomer containing parts of oil network, carboxylate groups, free fatty acids, metal ions and metal carboxylates. Reaction scheme was adapted from Hermans *et al.* (2019) [40].

1.3 Drier promoted curing reactions of oil

The curing reactions of oil are inherently slow; however, their rate can be enhanced in different ways. These may include increasing the concentration of reactive species, such as increasing the number of active sites and oxygen levels or by increasing the rate of initiation reactions by elevating the temperature, using irradiation, UV light, by the addition of pigments or more commonly by the addition of metal driers [2, 11, 22]. Among these, driers effectively cure the paint through multiple reactions (they may promote O_2 absorption, reduce induction time, and accelerate peroxide decomposition) [11, 45].

Paint driers can be classified based on their function: i) primary driers, also known as surface driers, which promote the oxidation reactions and ii) secondary driers, also known as through driers, which promote polymerization reactions and enhance the redox activity of the primary driers in bulk. To understand how different driers react, it is first important to remember that oxygen diffuses naturally through the oil from top to bottom, creating a gradient in the molecular oxygen concentration in the depth [11]. Different driers will influence how this oxygen acts, and this will impact the curing profile of the oil over the layer thickness. For instance, **primary driers**, such as Co^{2+}, Mn^{2+}, and Fe^{2+}, act at the paint surface. They are typically used at concentrations ranging from 0.005% to 0.2% relative to the binder or oil content. Initiation reactions described in Section 1.2 are slowed down by the presence of natural antioxidants in the binder. However, these reactions can be promoted by the addition of a primary drier. For instance, Soucek *et al.* (2012) propose that the primary Co^{2+} drier in its lower oxidation state reacts with O_2 and produces a metal superoxide coordination compound ($CoOO^{3+}$). This compound can then abstract an allylic or bis-allylic hydrogen atom and produce a hydroperoxide (R-OOH) and a carbon radical (R·). The hydroperoxide decomposition takes place via Haber–Weiss reaction, where the metal undergoes reversible cyclic redox reactions between two oxidation states differing by one electron (Figure 12) [11, 21, 22, 24]. In this process, alkoxy and peroxyl radicals are formed, which further react and form a highly cross-linked film [46]. When the alkoxy radicals react with other fatty acid molecules, alcohols are produced (R-OH) (Figure 12).

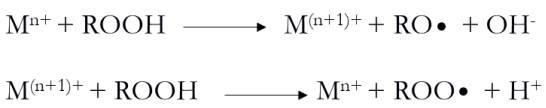

Figure 12. Drier promoted hydroperoxide decomposition in a Haber-Weiss redox reaction. The figure was adapted from Soucek *et al.* (2012) and Mallegol *et al.* (2000) [11, 24].

A detailed chemical scheme for drier-promoted curing is proposed by Gezici-Koç *et al.* (2016) [46].

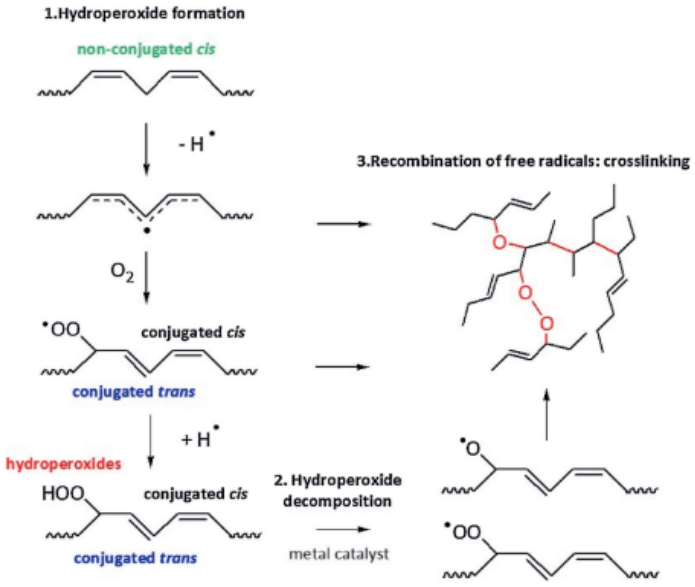

Figure 13. Reaction scheme of drier promoted hydroperoxide decomposition and cross-linking. Figure source is Gezici-Koç *et al.* (2016) [46].

Upon use of primary driers alone, the curing of the surface will occur first, forming a skin which lowers oxygen diffusion beneath the surface layer and causes wrinkling of the paint. Therefore, primary driers are commonly combined with secondary driers to obtain a fully cured paint film [11].

Secondary driers cannot initiate oxidative reactions like primary driers, but their metal ions can enhance the hydroperoxide decomposition (Figure 3, 5c, 9b, 12 and 13). Van Gorkum *et al.* (2005) classify all driers that are not primary driers as secondary driers, which are through driers, without additional classification to auxiliary driers, as it is unclear what auxiliary driers do on a molecular level [21]. However, Van den Berg (2002), Oyman (2005) and Soucek *et al.* (2012) classify the secondary driers as through and auxiliary, highlighting certain differences in their drier activity [2, 11, 22]. Pb^{2+}, Zr^{4+}, and Al^{3+} are considered through driers and, as the name suggests, they enhance cure in bulk [11, 21, 22]. They are considered as polymerizing driers. Furthermore, Soucek *et al.* (2012) mention that through driers may behave as Lewis acid co-catalysts to the surface driers [11].

Ca^{2+}, K^{+}, Li^{+}, and Zn^{2+} are auxiliary driers. These driers effectively stabilise primary driers by creating metal-oxygen bridges in the oil binder by the reaction with hydroxyl and carboxyl groups [2, 22, 45, 47]. Auxiliary driers delay the skinning process which ensures oxygen uptake through the film for a longer period of time. This process results in a harder film, better gloss, and reduced surface wrinkling. Auxiliary driers also prevent phase separation of surface and through driers from the polymeric phase [11].

Historical recipes frequently mention PbO - classified as a secondary drier - used on its own, most likely due to its through curing activity [11, 21]. In the following section, we review the most common historical formulations involving PbO and LO.

1.4 Historical evolution of driers: from Antiquity to today

1.4.1 Historical use of driers: huile de litharge

Lead compounds were commonly used in oil paintings for their curing properties from the 16th (with few earlier mentions) until the 20th century, when it was substituted with less toxic compounds. According to detailed analyses of historical painting recipes by Cotte *et al.* (2007, 2017 and 2019), litharge (PbO) was the most frequently used lead drier in oil paintings, followed by lead white and red lead (Pb_3O_4), which served both as pigments and driers [6, 42, 45, 47, 48]. Lead-tin yellow was also occasionally mentioned in historical formulations [6, 49, 50].

Litharge (α-PbO, red, tetragonal) and **massicot (β-PbO, yellow, orthorhombic)** are the two polymorphs of lead(II) oxide. Litharge was historically derived from the lead cupellation during smelting, while massicot was derived from litharge by heating to high temperatures, above 488 °C, where phase transition occurs. Litharge, massicot, and red lead may be derived by heating lead white for different durations at high temperatures (above 300 °C). Litharge may also be obtained from massicot at room temperature by mechanical treatment. PbO had various purposes throughout history (medical and building purposes), but it found its role in paintings as a drier [51].

In the literature, the term 'litharge' is sometimes used broadly to refer to both polymorphs, though strictly speaking, it refers only to the tetragonal form. The term "litharge" was first mentioned as *litargirio* in the Bologna manuscript in 1430: "*To make mordants for gilding on figures, on canvas, on stone, on wood, on gesso, and on mortar or walls. – Take* ***litharge (litargirio)****, verdisgris, and a little ocre, and grind them with a little linseed oil and liquid varnish; incorporate them well together, and then gild in the usual manner*" (cited according to Merrifield 1967, p.472) [47]. Litharge especially gained its popularity in the 17th and 18th centuries, due to its higher solubility in oil in comparison to other compounds [47]. Preparation and application of litharge in oil paintings is most commonly mentioned in the collection of recipes written by Théodore Turquet de Mayerne in the 17th century. One of the most notable recipes in the De Mayerne collection describes the preparation of ***huile de litharge***, often referred to as "thickened oil". This recipe consists of cooking PbO with oil at high temperatures, followed by water addition (Figure 14) [48, 52].

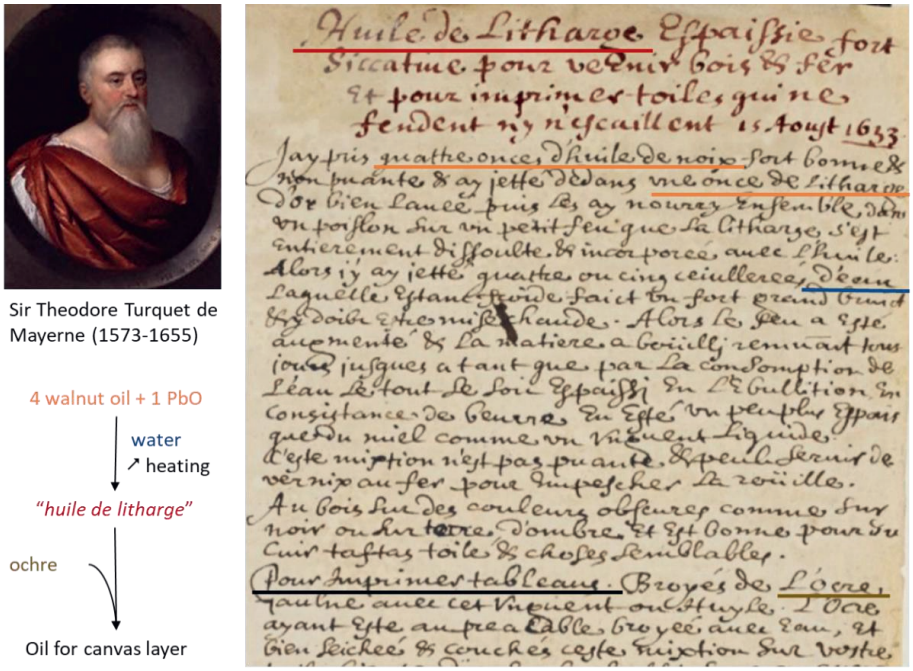

Figure 14. A historical recipe by Sir Theodore Turquet de Mayerne, 1633, on the preparation of leaded oil (*huile de litharge*). The figure was adapted from Cotte *et al.* 2017 [6].

Water addition allows to control the temperature and avoid burning, as well as to promote the hydrolysis of oil [6, 41]. Hydrolysis reaction releases more free fatty acids from the triglyceride ester, which turn the oil more acidic [40, 41]. PbO is a Brønsted base which can partially dissolve in the acidic oil by forming lead soaps (Figure 3, 9 and 13) [45, 47, 53]. The saponification rate is crucial, as the carboxylate ligand promotes miscibility of PbO in oil [11]. Lead soaps offer a source of Pb(II) which are the active species driving the decomposition of hydroperoxides [2, 11, 23, 45, 46]. Depending on the ligand involved, homolytic cleavage of either the O–O or -O-H bond results in the formation of alkoxy (R–O·) and peroxyl (R–O–O·) radicals (Figure 3, 9, 12 and 13) [22, 54]. As previously described in Section 1.2, these reactive radicals can participate in cross-linking reactions.

The saponified leaded oil medium was historically used to thicken the paint, enhance curing properties, pigment dispersion, film durability and stability [6, 45, 47]. Leaded oil medium was also used in combination with other organic binders (untreated oil, resin, wax) for the preparation of ground layers, glazes (transparent coloured oil paint layers), varnishes and in gilding [6, 45]. In his recipe, De Mayerne explicitly highlighted its use in panels and canvas impregnation to prevent splitting and flaking (Figure 14). Besides for its desirable properties on the paint, PbO was also favoured by artists for the low cost and availability [47].

1.4.2 Industrial materials

The use of PbO in oil mixtures has been extensively documented in historical treatises dating from the 16th century until the mid-20th century, when lead was substituted by less toxic and environmentally friendlier industrial driers [45]. Lead alternatives are zirconium, barium, bismuth and strontium, with zirconium being the most widely accepted replacement of lead [21]. While PbO was cooked at high temperature with LO to produce lead soaps (Section 1.4.1), industrial driers are synthesized as metal soaps by reacting metal compounds with natural or synthetic carboxylic acids such as linoleates, tallates, naphthenates and octoates. This is achieved through fusion at high temperatures, double decomposition/precipitation at lower temperatures, or direct metal reaction. The resulting metal carboxylates can be neutral, acidic or basic and are compatible with paint solvents and binders, enabling effective catalytic curing [11].

Besides the evolution of driers and the need for a healthier, more sustainable and environmentally friendly drier, binders also evolved from traditional drying oils to alkyd resins. At the beginning of the 20th century drying oils, including LO, were commercially pre-polymerized with temperature and driers to enhance their drying power. From 1940s, these pre-polymerized drying oils could not meet the industrial demand for a fast-curing medium with excellent properties [11, 21, 22, 55]. To obtain faster drying times, reduce yellowing and improve through-hardness, drying oils such as linseed, soybean, tung, safflower and dehydrated castor oil were partially substituted with alkyd resins [22]. Alkyd resins are polymeric binders derived from fatty acids, diacids such as phthalic acid and a polyol such as glycerol or pentaerythritol. Their widespread adoption in the paint and coatings industry is attributed to their improved curing performance, versatility across a range of substrates and applications, and better environmental and economic profiles [11, 55]. Like traditional drying oils, alkyd resins cure through oxidative polymerization (a mechanism discussed in the Section 1.2) [11].

Contemporary driers and binders continue to be developed with a focus on improving their sustainability and health safety. As a result, their chemical reactions are a common subject of scientific investigations, including an investigation of a novel, sustainable, photosensitive iron-based alkyd drier. This drier demonstrated improved performance, greater health compatibility, and an extended shelf life for industrial paints [56]. A part of this doctoral research is focused on the chemical reactivity and stability of this light-activated Fe-based drier using X-ray Absorption Near Edge Structure (XANES) and X-ray Fluorescence (XRF) techniques at beamline ID21 of the European Synchrotron Radiation Facility (ESRF). The results indicate that upon light activation, the Fe catalyst undergoes oxidation from Fe^{2+} to Fe^{3+}. These results are further discussed in the doctoral thesis by J. Bootsma (2024).

1.5 Sample corpus

1.5.1 Historical paint fragments

This thesis focuses mainly on micro-scale analyses, as macro-scale techniques offer limited spatial and chemical resolution, as well as lower sensitivity. In addition, these techniques have limitations in probing in-depth, which make it challenging to resolve the entire paint stratigraphy. To achieve a more detailed understanding of the spatial distribution of compounds, tiny paint fragments were collected for both laboratory-based and synchrotron radiation-based micro-scale analyses. The selection of samples in *The Night Watch* and *Mona Lisa* was determined based on the non-invasive macro-scale investigations. The samples of *The Last Supper* were already available. The acquired paint samples are several hundred microns in size and they were prepared for the analyses as raw (loose) fragments or embedded in resin. The method of preparation depends on both the requirements of the analytical technique and the specific research question being addressed. For instance, in Chapter 3, a loose micro-fragment of *Mona Lisa* painting was placed in a glass capillary (Ø = 500 μm) and analysed using synchrotron radiation high-angular resolution X-ray powder diffraction (SR-HR-XRPD, described in Section 1.6.2). In this case, the primary focus was to detect unusual crystalline lead compounds. Therefore, the embedding of the sample in resin and polishing was not needed, as spatial distribution was not in focus for such a small paint sample. Contrarily, in the case of *The Last Supper*, the goal was to visualize the distribution of crystalline lead-based compounds within a complex paint matrix using synchrotron radiation high-lateral-resolution 2D μ-XRPD mapping (SR-μ-XRPD, described in Section 1.6.2). To achieve this, the samples were embedded in epoxy resin and polished as cross-sections. The majority of the resin blocks were preserved for future analyses, while a smaller portion was sliced into thin sections using a microtome. Thin sectioning to ~ 10 μm for X-ray Powder Diffraction (XRPD) and < 4 μm for Fourier Transform Infrared (FTIR) spectroscopy, or alternatively, thinning the resin blocks to < 1 mm for XRPD, ensured optimal synchrotron beam transmission and prevented excessive absorption by the surrounding resin material.

1.5.2 Model paint fragments

To distinguish original materials, ageing or conservation-related products, and to elucidate the chemical formation pathways and kinetics of lead-based products in historical paintings requires model systems. For this purpose, simplified model systems based on PbO and LO were prepared following historical treatises, specifically the *huile de litharge* recipe by Turquet de Mayerne (described in Section 1.4.1, detailed in Chapters 2-4). Early formation and spatial distribution of lead-based products were studied on fresh (leaded) oil model systems. Part of the (leaded) oil media was applied on glass slides for spatial distribution analyses. To ensure the model system are representative of early drying stages in historical paintings, all samples were aged at room temperature (RT) for three years. However, the composition of models after several years of natural ageing is not comparable to the composition of a historical painting after several hundred years of natural ageing. To mimic the composition of historical paintings, model systems can be artificially aged in the laboratory by using UV light, elevated relative humidity and/or temperature, depending on the research question [57]. It is important to realise that the artificially aged models will never

truthfully represent the exact composition of the historical paintings. In this thesis one sample was artificially aged to observe the formation of lead-based products detected in historical paintings, over a prolonged period.

In addition, to assess the impact of synchrotron X-ray exposure on sensitive historical materials, model systems containing: (i) lead carbonate, (ii) lead chromate, and (iii) PbO in LO were prepared (detailed in Chapter 5). All model samples were prepared and analysed both as loose, unembedded fragments and as thin sections, depending on the requirements of the analytical technique and acquisition mode. All samples used in the radiation alteration study were naturally aged for periods ranging from one month to eight years.

1.6 Overview of methodologies: laboratory- and synchrotron-based techniques

Driers are typically added in small concentrations. Mallégol *et al.* (1999) report that less than 0.5% by weight of primary drier is needed to influence surface paint curing. Secondary driers, however, would require over 10% by weight to form complexes throughout the paint film [38]. Historical recipes indicate that 5% of PbO was added to the LO to create *huile de litharge* [45]. Unlike inert metal catalysts, driers like PbO actively react with oil components - especially free fatty acids - forming lead carboxylate complexes that readily dissolve in the oil matrix. Given the already low concentration of PbO in the complex paint matrix, it is likely that PbO is completely converted or reacted to trace amounts. The low concentrations and heterogeneous distribution of driers and their reaction products make them challenging to detect using traditional laboratory-based analytical techniques. To address this challenge, this thesis combines synchrotron radiation techniques - offering higher brilliance and precision - with laboratory-based methods. Additionally, we focus on the analyses of historical and model paint fragments using micro- and nano-probes suitable for analyses of paint fragments. Since paintings are composite materials containing both organic and inorganic, as well as amorphous and crystalline fractions, multiple analytical techniques were employed.

1.6.1 Laboratory-based analytical techniques

Optical microscopy was first used to visually inspect the samples, before the embedding and polishing, and before and after analyses. Visual investigation was particularly valuable for monitoring samples during preparation and for comparing visual modifications pre- and post-X-ray analyses in Chapter 5. A standard binocular optical microscopy and stereo-microscopy using Zeiss Axio microscope and a digital camera with magnifications ranging from 2.5× to 100× was used. Visible light microscopic images were documented using ZEN software to support further chemical analyses.

In **Scanning Electron Microscopy (SEM)**, a focused electron beam interacts with the surface of a paint micro-fragment, producing secondary electrons (SE), **backscattered electrons (BSE)** and characteristic X-rays. In paintings research, BSE imaging is mostly used to obtain information on the morphology and contrast in the composition, such as pigment distribution and layered structures based on atomic number differences. **Energy Dispersive X-ray Spectroscopy (EDS)** detects emitted X-rays, showing elemental composition relevant for distinguishing pigments and degradation products. Together, SEM-BSE and SEM-EDS provide detailed structural and chemical insights into paint composition. These techniques were used for the studies of historical paint fragments in Chapter 3.

Fourier Transform Infrared spectroscopy (FTIR) is commonly used in heritage science to study organic fractions and pigment composition, as well as the newly-formed products, such as metal soaps by analysing the characteristic vibrational frequencies of their functional groups [40, 43, 58, 59]. In this thesis, FTIR spectroscopy was used to study the composition of historical paints, as well as to follow the PbO and LO chemical reactions in model systems and identify their reaction products.

Micro-FTIR (μ-FTIR) combines FTIR coupled with a microscope. This method is particularly useful for spatially resolved identification of components in complex and multi-layered paint matrices. μ-FTIR can operate in reflection and in transmission mode. For the transmission mode, the sample should be sufficiently thin to allow the beam to pass through it and to avoid signal oversaturation. For this purpose, samples are usually prepared as transversal thin sections with thickness selected based on their composition. In this thesis, μ-FTIR spectroscopy was used to investigate the composition of naturally and oven aged model systems, as well as to assess their molecular radiation-induced alteration after exposure to different X-ray conditions (Chapters 2 and 5).

Attenuated Total Reflectance Micro-FTIR (ATR-μ-FTIR) improves surface sensitivity by using a high-refractive-index crystal to generate an evanescent wave that detects molecular absorption near the surface. This analysis is recommended for non-destructive, high spatial resolution analysis without the need for extensive sample preparation or thickness. Both μ-FTIR and ATR-μ-FTIR modes offer visualization of the spatial distribution of specific compounds in an integrated intensity map, by using region of interest (ROI) imaging tool. In this thesis, ATR-μ-FTIR mapping was used for the study of historical fragments (Chapter 3).

Bulk Attenuated Total Reflectance (ATR-FTIR) is suited for analysing larger samples where spatial distribution is not the primary focus. In this thesis, for instance, bulk ATR-FTIR is also applied to liquids, such as fresh model systems (leaded) oil media, to investigate the early stage curing reactions (Chapter 4).

Headspace Solid-Phase Microextraction Gas Chromatography Mass Spectrometry (HS-SPME-GC-MS) is a non-destructive technique used to analyse volatile organic fractions often formed in paintings. In this research, HS-SPME-GC-MS was employed to detect the volatile short-chain fatty acids in fresh model reconstructions with the aim of elucidating the chemical reactions of LO cooked with and without PbO and water. For HS-SPME-GC-MS, a fiber coated with an adsorbent material captures volatile compounds from the painting's surface or its surrounding in a closed environment. These compounds are then desorbed into a mass spectrometer for identification. For instance, in this thesis HS-SPME-GC-MS was used to detect free formic acid in pure LO and leaded oil systems (Chapter 4).

Matrix-Assisted Laser Desorption/Ionization Mass Spectrometry Imaging (MALDI-MSI) is a cutting-edge technology tool for two-dimensional mass spectrometry that can visualize the spatial distribution of molecules without extraction, purification, and separation of the sample and its components. It is a soft ionisation technique that uses a laser for desorption and sublimation of the analyte. A matrix is sprayed or deposited over the sample, which absorbs the laser energy to prevent fragmentation of the analyte molecules by direct laser light. The matrix desorbs and facilitates the ionisation of the molecules of interest. After collecting a mass spectrum at one spot, the sample is moved to reach another region, and so on, until the entire sample is scanned in a raster format. In the resulting spectra a selection of masses that corresponds to the studied compounds, can be made to map their respective distributions across a multi-layered sample. In this thesis, MALDI-MSI was used for the first time to map molecular alterations in model systems due to exposure to SR-μ-XRPD mapping in Chapter 5.

1.6.2 Synchrotron-based analytical techniques

The samples investigated in this thesis are of exceptional significance and limited in size and quantity. To maximise the analytical yield from these micro-fragments, advanced high-resolution X-ray micro- and nano-scale probe techniques were required. Synchrotron radiation-based methods are particularly suited to this task due to their increased resolution, selectivity and sensitivity. Before detailing the individual synchrotron techniques applied in this research, it is essential to first outline the basic principles of synchrotron radiation and their advantages for the historical material studies. In the following section we present the specifications for ESRF.

Basic principles of synchrotron-based radiation

To generate synchrotron radiation, bunches of electrons are first generated and emitted by an electron gun at the start of the linear accelerator (linac) (Figure 15A). They are gradually accelerated using electric fields until they reach an energy of 200 million electron-volts (MeV), bringing them close to the speed of light. These electrons are then injected into the smaller ring called a booster synchrotron, which in the case of ESRF, has a circumference of 300 metres (Figure 15B). With each lap around the booster synchrotron, the electrons gain more energy until they reach the final energy of 6 GeV. Once they reach this energy they travel to the storage ring which has a circumference of 844 meters and operates within an ultra-high vacuum environment ($\sim 10^{-9}$ mbar) (Figure 15C). Inside the storage ring, the electrons pass through a series of magnets, including bending magnets, undulators, and focusing magnets. Bending magnets curve the path of tangentially emitted electrons to follow the circular path and direct them towards the beamlines. Insertion devices such as undulators and wigglers, consist of a series of small magnets with alternating polarity force the electrons onto a sinusoidal path, producing intense, bright, and coherent X-rays. Focusing magnets focus the beam as narrow as possible. The generated X-rays are then directed to different laboratories known as beamlines, each designed for specific experimental technique and research purpose (Figure 15D). Some beamlines have a monochromator which is used to separate and select different wavelengths of the synchrotron light for the experiments. Nano- and micro-X-ray focusing beamlines utilise either two perpendicular

mirrors, called Kirkpatrick–Baez (KB) mirrors or compound refractive lenses (CRLs) to focus the X-ray beam.

Synchrotron light is extremely bright, orders of magnitude brighter than a conventional lab source. This makes it highly intense (>10^{12} photons per second), small and collimated, which makes it ideal for the micro- and nano-scale analyses of tiny and complex paint samples (hundreds of μm in size). Additionally, the synchrotron light offers tunability of energy (from X-rays to infrared) which is required for absorption spectroscopy techniques, and it also offers imaging capacities, down to a sub-micrometric resolution which is particularly suited for the analyses of composite, heterogeneous and multi-layered matrices.

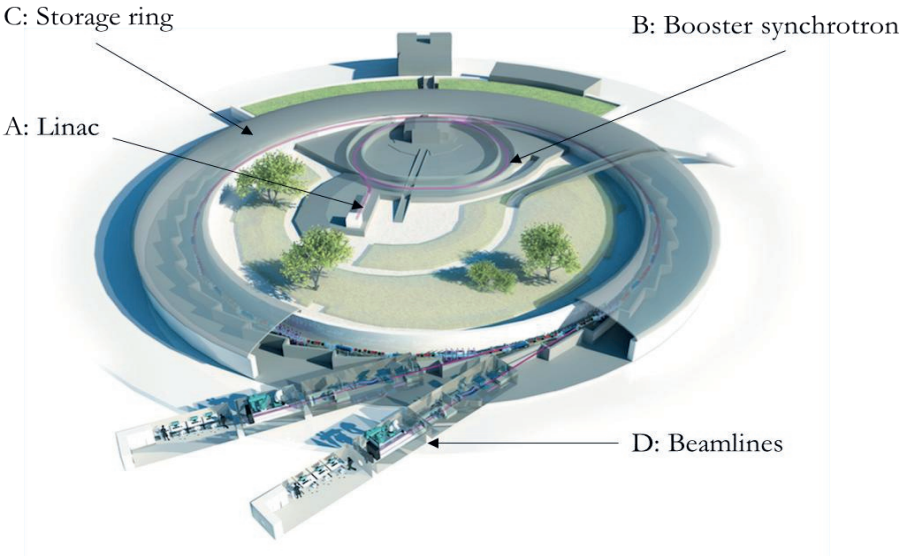

Figure 15. Schematic illustration of a synchrotron facility based on the European Synchrotron Radiation Facility: A: Linear accelerator or linac; B: Booster synchrotron; C; Storage ring and D: Beamlines [60].

European Synchrotron Radiation Facility and the Historical Materials Block Allocation Group (BAG)

As of 2022, there are approximately 60 synchrotron light sources operating worldwide. One of those light sources is the European Synchrotron Radiation Facility (ESRF), located at the South of France, in Grenoble.

For the past 20 years, ESRF hosted a large community of heritage scientists, who regularly exploited the X-ray-based techniques, including X-ray fluorescence (XRF), X-ray absorption spectroscopy (XAS) and XRPD. These techniques may be used alone or combined for the analysis of micro-samples of cultural heritage materials [61]. X-ray based analyses may offer us information on the current composition and condition of objects. This information can tell us more on the

object's manufacturing techniques and the evolution of materials over time. Based on this information, conservators develop adequate conservation and restoration methods for the long-term preservation of the objects for future generations.

Cultural heritage community at ESRF uses several beamlines for their research through the standard user programme, which consists of writing the standard two-page proposals, planning the experiment, setting-up beamtime. The most commonly used beamlines through the standard user programme are the newly developed BM18, dedicated to X-ray tomography for large, high-energy and high-coherence imaging, and BM05, both offering X-ray computed tomography (CT) largely used to scan fossils, and the micro-spectroscopy beamline ID21 dedicated to XAS.

In addition to the standard user program, cultural heritage users at the ESRF regularly exploit the capabilities of ID13 and ID22 beamlines through the newly established Historical Materials Block Allocation Group (BAG). This shared access mode was introduced following the 2020 upgrade of the ESRF to an Extremely Brilliant Source (EBS), which significantly enhanced beam brightness and coherence. Coupled with advancements in beamline instrumentation, these improvements have increased the speed and efficiency of analyses. The increased speed of analyses offered the opportunity to analyse hundreds of samples within a few days of beamtime, i.e. far more than what cultural heritage researchers commonly need. To address this, ESRF researchers introduced a novel and sustainable approach: combining multiple short (<1 shift) proposals from different cultural heritage groups into a single proposal, under a requirement that they need XRPD techniques. Synchrotron radiation XRPD is one of the most informative techniques when it comes to the study of the crystalline nature of cultural heritage objects. It not only offers the opportunity to identify the crystalline phases within complex matrices, but also to assess their crystallite size, microstrain, orientation and crystal structure. High demand for XRPD and improved capacities offered by European Synchrotron Radiation Facility-Extremely Brilliant Source (ESRF-EBS), motivated the Historical Materials BAG access mode, granting users access to two specialized X-ray diffraction beamlines: ID22 and ID13. XRPD data shown in this thesis was mostly produced through the BAG access. We have regularly employed the advanced capacities of high-angular resolution SR-HR-XRPD at ID22 and high-lateral-resolution 2D SR-μ-XRPD mapping at ID13, as each BAG beamtime occurs every six months.

Over the past five years, the initiative has proven highly successful, generating significant scientific insights in heritage science, attracting and training new users in synchrotron science, offering more flexibility in the choice of projects and fostering a strong international research network [62].

X-ray Powder Diffraction (XRPD)

X-ray Powder Diffraction (XRPD) is an analytical technique used to identify the crystalline phases in materials based on how they diffract X-rays. When an X-ray beam interacts with the crystalline material, it is diffracted in specific directions through constructive interference of scattered X-rays from sets of lattice planes, characterized by the Miller indices (*hkl*). Parallel planes that are equally distanced (d_{hkl}) share the same indices. When the extra distance travelled by the scattered X-rays is equal to a whole number (n) of wavelengths (λ), they interfere constructively. This principle of X-

ray diffraction is explained by the Bragg's law: $n\lambda = 2d \sin\theta$, where n is an integer number of the order of the diffracted beam, λ is the wavelength of the incident X-rays, d (also known as d-spacing) is the distance between planes of atoms, and θ is the angle of diffraction, between the lattice plane and the diffracted X-ray beam. The angle between incident and diffracted beam is 2θ. The constructive interference of X-rays leads to strong intensity maxima in a diffraction pattern characteristic of the crystalline structure. Angles (θ) and intensities of the diffracted X-rays are characteristic of the crystalline structures. Additionally, the diffraction pattern yields information about the orientation and size of the crystals [63]. The amount of broadening of XRPD peaks (Full Width Half Maximum, FWHM) can be used to determine the crystallite size [64].

High-angular resolution X-ray powder diffraction (SR-HR-XRPD)

SR-HR-XRPD at ID22 relies on an X-ray source with energies ranging from 6 to 80 keV, utilising the ESRF-EBS capacities. For the study of historical materials within the BAG group, the energy was standardized to 35 keV to reduce the beam overabsorption by the sample and avoid radiation alteration. The X-ray beam at ID22 is highly monochromatic of low divergence, with diffracted photons measured using an EIGER2 2M-W CdTe pixel detector behind 13 Si(111) analyser crystals. This setup ensures high precision XRPD measurements. This bulk (beam size ~1 × 1 mm^2) XRPD technique offers identification and quantification of the crystalline materials, structure refinement and crystallite size assessment and description of the crystallographic structure. It is particularly effective for detecting small variations in the lattice parameter, which can be attributed to factors such as strain, doping, or other influences. Additionally, it is suitable for fast screening of modern reproductions that have been exposed to artificial aging, allowing for efficient analysis of material degradation or changes over time. At ID22, samples can be analysed as powders or loose fragments placed in borosilicate glass capillaries of different diameters. The size of the capillary for powders depends on the sample composition and X-ray absorption coefficient [62]. This technique was used for the detection of crystalline phases in *Mona Lisa* fragment in Chapter 3.

Synchrotron radiation micro-X-ray powder diffraction (SR-μ-XRPD)

In comparison to SR-HR-XRPD, SR-μ-XRPD offers spatially resolved identification of the crystalline phases in historical materials. ID13 has two end-stations: a micro-branch (~2 × 2 μm^2 beam size) and a nano-branch (beam size down to 100 nm), operated in time-sharing mode. For the BAG group experiments, the micro-branch is preferred due to its larger beam size, which is more suitable for powder diffraction when crystallites are smaller than the beam, and the ability to scan larger samples. The beamline enables simultaneous XRF and XRPD measurements using a Vortex EM detector. The beam energy at ID13 ranges from 5 to 30 keV but for the purpose of the BAG experiments, it is typically set to ~13.0 keV, to slightly excite the Pb L3-edge without XRF oversaturating the detector or affecting transmission. The beam is focused to ~2 × 2 μm^2 (flux ~2 × 10^{12} ph/s, at I = 128 mA electron beam current) using a compound refractive lens set-up (CRL) mounted in a transfocator.

XRPD maps are obtained by raster-scanning samples and collecting 2D patterns with a Dectris EIGER 4 M single photon counting detector that acquires frames with 2070 × 2167 pixels (75 × 75 μm^2 pixel size) at a rate up to 750 Hz. The measurements are conducted in transmission mode, with samples prepared as thin sections, typically ~10 μm thick, and mounted vertically, perpendicular to the beam [62, 65]. In this thesis, SR-μ-XRPD mapping was regularly used to detect the crystalline phases in aged historical and model systems, as well as to assess *in-situ* X-ray alteration in model systems (Chapters 2-5).

Synchrotron X-ray beam-induced alterations

While synchrotron radiation X-ray-based techniques have proven invaluable for analysing historical materials, it is important to acknowledge that they can induce optical, molecular, and structural alterations in fragile micro-fragments, which are often limited in size and number. X-ray radiation-induced changes are a common concern among researchers and especially conservators in charge of the preservation of both the object and micro-fragments as integral parts of the artwork. This challenge in synchrotron analysis of historical materials has motivated us to reconsider our operating conditions with precious historical materials. For instance, during the first BAG experiments at ID13 using higher intensity conditions offered by the ESRF-EBS, we tested different measurement parameters on mock-ups to avoid radiation alteration. The flux was modulated by detuning the undulators to reduce radiation alteration of beam sensitive samples. In addition to this, dwell time was optimized as well to minimise sample modification. These challenges further motivated the study of radiation-induced alterations described in Chapter 5. The experimental protocol used in this study combined μ-XRPD with μ-FTIR and MALDI-MSI to assess synchrotron X-ray radiation primarily on mock-up paints containing different pigments and binders, representative of historical systems.

1.7 Research approach

Overall, this thesis focuses on the leaded oil chemical interactions of PbO and LO using laboratory- and synchrotron-based analyses. The first two chapters of this thesis explore the presence of uncommon lead products in historical paintings, while the third chapter investigates their early formation and detection in more detail through leaded oil model systems. The last chapter focuses on the assessment of synchrotron X-ray sample alteration for safe analyses.

Chapter 2 investigates the unexpected presence and spatial distribution of lead(II) formate (LF) in Rembrandt's *The Night Watch* through a multi-scale analytical approach. For the first time, MA-XRPD analyses have identified LF in a historical painting, primarily in light-toned, lead-white-rich areas, and in one case, in a lead-tin yellow-rich region. Given the sensitivity and penetration depth limitations of MA-XRPD, further micro-scale analyses were essential to determine whether LF is an original component, a conservation-related by-product, or a result of paint ageing. To address this, micro-fragments were collected from the painting and analysed using optical microscopy, SR-μ-XRPD and ATR-μ-FTIR. To explore the formation and stability of LF in historical oil paintings, leaded oil-based model paint systems were synthesized based on historical treatises. These model systems were analysed as loose, unembedded fragments and thin sections, fresh and aged for three years at room temperature using optical microscopy, SR-μ-XRPD and transmission μ-FTIR spectroscopy. The results obtained on both historical and model systems were compared.

In **Chapter 3**, ground layers of Leonardo da Vinci's *Mona Lisa* were studied. MA-XRF and X-ray radiography of the painting revealed new insights on the stratigraphy of the painting, specifically on the lead distribution in the ground layers. To investigate the composition of this layer, a single minute paint fragment was collected from the ground layer of the painting. One part was analysed using optical microscopy, SEM-EDS and ATR-μ-FTIR, while the other was preserved for SR-HR-XRPD analysis. To gain a deeper understanding of Leonardo's palette, we also examined samples from *The Last Supper* using SR-μ-XRPD and SR-ATR-μ-FTIR. To obtain more insight into the potential composition of ground layers of both artworks, leaded oil model systems based on historical recipes were analysed using SR-μ-XRPD. In addition to the scientific analyses, a comprehensive review of Leonardo's treatises provided valuable insights into his materials and techniques.

Chapter 4 consists of an in-depth study of the early formation and detection of unusual lead products, including LF, lead formate hydroxide (LFH), plumbonacrite (PN), shannonite (SH) and neo-formed hydrocerussite (nHCer). A detailed literature review highlighted that these lead-containing compounds were not always systematically detected and are often heterogeneously distributed in both historical and model paintings. To address this rare detection and heterogeneous distribution, simplified leaded oil model systems were prepared based on historical recipes. The low concentrations and heterogeneous spatial distribution of these reaction products in complex paint matrices required careful consideration of the analytical approach. In this study, we combined bulk and spatially resolved laboratory- and advanced synchrotron-based techniques, notably optical microscopy, HS-SPME-GC-MS, ATR-FTIR, μ-FTIR and SR-μ-XRPD to detect and map the presence of unusual lead-based compounds in our model systems.

Chapter 5 focuses on the assessment of the impact of synchrotron radiation (SR) on historical and model paints during X-ray micro-analyses. Specifically, this study aims to (i) distinguish between original materials and radiation-induced alteration products in model systems layers representative of historical paints and (ii) assess the extent of structural and molecular alteration using *in-situ* SR-μ-XRPD probe and an *ex-situ* μ-FTIR probe. To achieve this, mock-up samples representative of historical paintings were synthesized, containing various pigments, including lead carbonates, lead chromate, and PbO mixed with LO. These samples were aged for different periods (from one month to eight years) with the aim to assess their modification with respect to that of historical artworks. A multi-analytical approach was employed: optical microscopy for the documentation of visual alterations before and after X-ray exposure, SR-μ-XRPD for the *in-situ* monitoring of structural changes in pigments during exposure to synchrotron radiation, MALDI-MSI and μ-FTIR for *ex-situ* assessment of molecular changes, particularly in organic oil binders. Given the large dataset generated in this study (tens of thousands of FTIR spectra), a customized Orange workflow was developed to efficiently process and analyse the data. Principal Component Analysis (PCA) was applied to identify the trends in radiation-induced modifications and explore how different factors, such as age and level of cross-linking impact sample sensitivity to X-rays.

Chapter 6 gives the conclusion of and reflection on the overall thesis and the future perspectives related to the lead-containing reaction products in oil paintings and synchrotron X-ray radiation alteration studies. In this chapter, we also address the contribution of the studies to the field in a wider context and significance for future conservation practices.

1.8 References

[1] Berg, J. D. J. V. D. and Boon, J. J. Chemical changes in curing and ageing oil paints. *Icom Committee For Conservation,* **1**, 248-253 (1999).

[2] Berg, J. D. J. V. D. *Analytical chemical studies on traditional oil paints*. 1-291 [PhD thesis] University of Amsterdam (2002).

[3] Stutz, G. F. A. Some Effects of ultra-Violet Light on Paint Vehicles[1]. *Ind. Eng. Chem.* **18**, 1235–1238 (1926).

[4] Rasti, F. and Scott, G. Mechanisms of antioxidant action: The role of copper salts in the photostabilization of paint media. *Eur. Polym. J.* **16**, 1153–1158 (1980).

[5] Mazzeo *et al.* Attenuated total reflection micro FTIR characterisation of pigment-binder interaction in reconstructed paint films. *Anal. Bioanal. Chem.* **392**, 65–76 (2008).

[6] Cotte, M. *et al.* Lead soaps in paintings: Friends or foes? *Stud. Conserv.* **62,** 2–23, (2017).

[7] Gonzalez, V. *et al.* Unraveling the Composition of Rembrandt's *Impasto* through the Identification of Unusual Plumbonacrite by Multimodal X-ray Diffraction Analysis. *Angew. Chem.* **131**, 5675–5678 (2019).

[8] Švarcová, S. *et al.* Uncovering lead formate crystallization in oil-based paintings. *Dalton Trans.* **49**, 5044–5054 (2020).

[9] Garrappa *et al.* Initial stages of metal soaps` formation in model paints: The role of humidity. *Microchem. J.* **156**, 104842 (2020).

[10] Vanmeert, F., Vandersnickt, G., and Janssens, K. Plumbonacrite identified by X-ray powder diffraction tomography as a missing link during degradation of red lead in a van Gogh painting. *Angew. Chem. - Int. Ed.* **54**, 3607–3610 (2015).

[11] Soucek, M. D., Khattab, T., and Wu, J. Review of autoxidation and driers. *Prog. Org. Coat.*, **73**, 435–454 (2012).

[12] Lazzari, M. and Chiantore, O. Drying and oxidative degradation of linseed oil. *Polymer Degradation and Stability*. **65,** 303-313 (1999).

[13] Bonaduce, I. *et al.* Conservation issues of modern oil paintings: a molecular model on paint curing. *Acc. Chem. Res.* **52**, 3397–3406 (2019).

[14] Izzo, F. C. *20th Century Artist's Oil Paints; A Chemical-Physical Survey*. 1-218 [PhD thesis] (2009).

[15] Franken *et al.* Set Back the Race: Treatment Strategies for Running Oil Paint. (In *Issues in Contemporary Oil Paint*, van den Berg, K. J., Burnstock, A., de Keijzer, M., Krueger, J., Learner, T., de Tagle, A., and Heydenreich, G.) 333–349 (Springer International Publishing, 2014).

[16] Boon, J. J. and Hoogland, F. G. Investigating Fluidizing Dripping Pink Commercial Paint on Van Hemert's Seven-Series Works from 1990–1995. (In *Issues in Contemporary Oil Paint*, van den Berg, K. J., Burnstock, A., de Keijzer, M., Krueger, J., Learner, T., de Tagle, A., and Heydenreich, G.) 227-246 (Springer International Publishing, 2014).

[17] La Nasa, J. *et al.* Novel application of liquid chromatography/mass spectrometry for the characterization of drying oils in art: Elucidation on the composition of original paint materials used by Edvard Munch (1863–1944). *Anal. Chim. Acta*, **896**, 177–189 (2015).

[18] Tumosa, C. S. and Mecklenburg, M. F. The influence of lead ions on the drying of oils. *Stud. Conserv.* **50**, 39-47 (2005).

[19] Fjällström, P., Andersson, B., Nilsson, C., and Andersson, K. Drying of linseed oil paints: a laboratory study of aldehyde emissions. *Industrial Crops and Products.* **16**, 173–184 (2002).

[20] Juita, Dlugogorski, B. Z., Kennedy, E. M., and Mackie, J. C. Low temperature oxidation of linseed oil: a review. *Fire Sci. Rev.* **1**, 3 (2012).
[21] Van Gorkum, R. and Bouwman, E. The oxidative drying of alkyd paint catalysed by metal complexes. *Coord. Chem. Rev.* **249**, 1709–1728 (2005).
[22] Oyman, Z. O. *Towards Environmentally Friendly Catalysts For Alkyd Coatings*. Technische Universiteit Eindhoven. 1-183 [PhD thesis] (2005).
[23] De Polo, G., Iedema, P., Shull, K., and Hermans, J. Comprehensive Characterization of Drying Oil Oxidation and Polymerization Using Time-Resolved Infrared Spectroscopy. *Macromolecules*. **57**, 8263–8276 (2024).
[24] Mallégol, J., Lemaire, J., and Gardette, J.-L. Drier influence on the curing of linseed oil. *Progress in Organic Coatings*. **39**, 107–113 (2000).
[25] Muizebelt, W. J., Hubertb, J. C., and Venderboschb, R. A. M. Mechanistic study of drying of alkyd resins using ethyl linoleate as a model substance. *Progress in Organic Coatings*. **24**, 263-279 (1994).
[26] Powers, P. O. Mechanism of the Oxidation of Drying Oils. Industrial and Engineering Chemistry. **41**, 304-309 (1949).
[27] Privett, O. S. Autoxidation and autoxidative polymerization. *J. Am. Oil Chem. Soc.* **36**, 507–512 (1959).
[28] Ingold, K. U. Inhibition of the Autoxidation of Organic Substances in the Liquid Phase. *Chem. Rev.* **61**, 563–589 (1961).
[29] Morris, S. G. Recent Studies on the Mechanism of Fat Oxidation in Its Relation to Rancidity. *J. Agric. Food Chem.* **2**, 126–132 (1954).
[30] Frankel, E. N. Volatile Lipid Oxidation Products. *Prog. Lipid Res.* **22**, 1-33 (1982).
[31] Frankel, E. N. Lipid Oxidation. *Prog. Lipid Res*. **19**, 1-22 (1980).
[32] Swern, D. and Coleman, J. E. Reactions of Fatty Materials with Oxygen. XX. Recent developments in the autoxidation of methyl oleate and other monounsaturated fatty materials. *J. Am. Oil Chem. Soc.* **32**, 700–703 (1955).
[33] Wexler, H. Polymerization Of Drying Oils. *Chem. Rev.* **64**, 591–611 (1964).
[34] Zhang, W., Shi, B., and Shi, J. A Theoretical Study On Autoxidation Of Unsaturated Fatty Acids And Antioxidant Activity Of Phenolic Compounds. *JALCA*, **102**, 99-105 (2007).
[35] Meilunas, R. J., Bentsen, J. G. and Steinberg, A. Analysis of Aged Paint Binders by FTIR Spectroscopy. *Stud. Conserv.* **35**, 33–51 (1990).
[36] Pizzimenti *et al.* Oxidation and Cross-Linking in the Curing of Air-Drying Artists' Oil Paints. *ACS Appl. Polym. Mater.* **3**, 1912–1922 (2021).
[37] Baij, L., Chassouant, L., Hermans, J. J., Keune, K., and Iedema, P. D. The concentration and origins of carboxylic acid groups in oil paint. *RSC Adv.* **9**, 35559–35564 (2019).
[38] Mallégol, J., Gardette, J.L., and Lemaire, J. Long-Term Behavior of Oil-Based Varnishes and Paints I. Spectroscopic Analysis of Curing Drying Oils. *JAOCS*, **76**, 967-976 (1999).
[39] Chiniwalla, P. *et al.* Crosslinking and decomposition reactions of epoxide functionalized polynorbornene. Part I. FTIR and thermogravimetric analysis. *J. Appl. Polym. Sci.*, **89**, 568–577 (2003).
[40] Hermans, J. J., Keune, K., Van Loon, A. and Iedema, P. D. In *Metal Soaps in Art* (eds Casadio, F. *et al.*) 47–67 (Cham, Springer, 2019).

[41] Tumosa, C. S. and Mecklenburg, M. F. Oil Paints: The Chemistry of Drying Oils and the Potential for Solvent Disruption. (In New Insights into the Cleaning of Paintings: Proceedings from the Cleaning 2010 International Conference, Universidad Politecnica de Valencia and Museum Conservation Institute, eds. Mecklenburg, M. F., Charola, A. E., and Koestler, R. J.) 51–58 (Smithsonian Institution, Washington, DC, Smithsonian Contributions to Museum Conservation, 2013).

[42] Casadio, F. *et al., Metal Soaps in Art* (Springer, 2019).

[43] Hermans, J. J., Keune, K., Van Loon, A., Corkery, R. W., and Iedema, P. D. Ionomer-like structure in mature oil paint binding media. *RSC Adv.*, **6**, 93363–93369 (2016).

[44] Keune, K. and Boon, J. J. Analytical imaging studies of cross-sections of paintings affected by lead soap aggregate formation. *Stud. Conserv.*, **52**, 161–176 (2007).

[45] Viguerie, L. D., Payard, P. A., Portero, E., Walter, P. and Cotte, M. The drying of linseed oil investigated by Fourier transform infrared spectroscopy: Historical recipes and influence of lead compounds. *Prog. Org. Coat.* **93**, 46–60 (2016).

[46] Gezici-Koç, Ö. *et al.*, In-depth study of drying solvent-borne alkyd coatings in presence of Mn- and Fe- based catalysts as cobalt alternatives. *Mater. Today Commun.*, **7**, 22–31 (2016).

[47] Zumbühl, S. and Zindel, C. In *Historical siccatives for oil paint and varnishes*. (eds Zumbühl, S. & Zindel, C.) 6-21 (Bern, HDW Publications Bern, Research for Conservators, 2022).

[48] Cotte, M., Checroun, E., Susini, J., and Walter, P. Micro-analytical study of interactions between oil and lead compounds in paintings. *Appl. Phys. Mater. Sci. Process.*, **89**, 841–848 (2007).

[49] Keune, K., *Binding medium, pigments and metal soaps characterised and localised in paint cross-sections*. in MolArt, no. 11. Amsterdam: FOM Institute for Atomic and Molecular Physics, 1-182 [PhD thesis] (2005).

[50] Higgitt, C., Spring, M. and Saunders, D. Pigment-medium interactions in oil paint films containing red lead or lead-tin yellow, *National Gallery Technical Bulletin*. **24**, 75-95 (2003).

[51] Gliozzo E. and Ionescu C. Pigments-Lead-based whites, reds, yellows and oranges and their alteration phases. *Archaeol. Anthropol. Sci.* **14**, 17 (2022).

[52] Cotte, M. *et al.* Kinetics of oil saponification by lead salts in ancient preparations of pharmaceutical lead plasters and painting lead mediums. *Talanta*, **70**, 1136–1142 (2006).

[53] Gonzalez, V. *et al.* X-ray and Infrared Microanalyses of Mona Lisa's Ground Layer and Significance Regarding Leonardo da Vinci's Palette. *J. Am. Chem. Soc.* **145**, 23205–23213 (2023).

[54] Chavez, F. A. and Mascharak, P. K. Co(III)−Alkylperoxo Complexes: Syntheses, Structure−Reactivity Correlations, and Use in the Oxidation of Hydrocarbons. *Acc. Chem. Res.*, **33**, 539–545 (2000).

[55] Hofland, A. Alkyd resins: From down and out to alive and kicking. *Prog. Org. Coat.* **73**, 274–282 (2012).

[56] Bootsma, J., Browne, W. R., Flapper, J. and De Bruin, B. Photoactive Fe Catalyst for Light-Triggered Alkyd Paint Curing. *JACS Au*, **2**, 531–540 (2022).

[57] Izzo, F. C., Balliana, E., Perra, E. and Zendri, E. Accelerated Ageing Procedures to Assess the Stability of an Unconventional Acrylic-Wax Polymeric Emulsion for Contemporary Art," *Polymers*. **12**, 1925 (2020).

[58] Derrick, M. R., Stulik, D. and Landry, J. M. Infrared spectroscopy in conservation science, 1-235 (In *Scientific tools for conservation*, Los Angeles: Getty Conservation Institute, 1999).

[59] Hermans, J. and Helwig, K. The Identification of Multiple Crystalline Zinc Soap Structures Using Infrared Spectroscopy. *Appl. Spectrosc.* **74**, 1505–1514 (2020).

[60] Accelerators. ESRF. *https://www.esrf.fr/home/UsersAndScience/Accelerators.html*

[61] Cotte, M. *et al.* New opportunities offered by the ESRF to the cultural and natural heritage communities. *Synchrotron Radiat. News*. **35**, 3–9 (2022).

[62] Cotte, M. *et al.* The 'Historical Materials BAG': A New Facilitated Access to Synchrotron X-ray Diffraction Analyses for Cultural Heritage Materials at the European Synchrotron Radiation Facility. *Molecules*, **27**, 1997 (2022).

[63] Dinnebier, R. E. and Billinge, S. J. L. in *Powder Diffraction: Theory and Practice* (ed. R. E. Dinnebier and S. J. L. Billinge) 1-19 (Cambridge, *The Royal Society of Chemistry,* 2008).

[64] Gonzalez, V., Cotte, M., Vanmeert, F., de Nolf, W. and Janssens, K. X-ray Diffraction Mapping for Cultural Heritage Science: a Review of Experimental Configurations and Applications. *Chemistry - A European Journal*, **26**, 1703–1719 (2020).

[65] Riekel, C., Burghammer, M., and Davies, R. Progress in micro- and nano-diffraction at the ESRF ID13 beamline. *IOP Conf. Ser. Mater. Sci. Eng.* **14**, 012013 (2010).